RSC Advances

PAPER

View Article Online
View Journal | View Issue

Cite this: *RSC Adv.*, 2016, **6**, 101707

Controlling red upconversion luminescence in Gd_2O_3:Yb^{3+}–Er^{3+} nanoparticles by changing the different atmosphere†

Shengjun Zhang,[a] Jiajia Zhou,*[ab] Ruozhen Wu,[a] Lei Lei,[a] Zhen Xiao,[a] Junjie Zhang[a] and Shiqing Xu*[a]

Received 12th September 2016
Accepted 11th October 2016

DOI: 10.1039/c6ra22754f

www.rsc.org/advances

Lanthanide (Ln^{3+})-doped nanoparticles that produce strong red upconversion (UC) luminescence are desirable for biological applications. For nanoparticles, modification of their electronic properties and stabilization of their crystallographic phase are crucial for tuning their luminescence behaviors. Here, Yb^{3+}–Er^{3+} doped Gd_2O_3 nanoparticles have been synthesized by calcining Gd_2O_2S in nitrogen (O_2-free) and ambient air (~21% O_2), respectively. Various approaches including X-ray diffraction (XRD), transmission electron microscopy (TEM), Raman spectroscopy and thermo-gravimetric and differential thermal analyses (TG-DTA) were used to characterize the structure, morphology and phase formation mechanism of the nanoparticles. Upconversion luminescence properties were investigated by emission intensity *vs.* excitation power (double logarithmic relationship) and temperature dependent emission spectroscopy. The different splitting transition probabilities of the cubic and/or monoclinic phase, the probability of multiphonon relaxations and cross relaxations between Er^{3+} ions are responsible for the efficient red emission in the cubic Gd_2O_3 nanoparticles. More importantly, the lower phonon energy of the pure cubic sample has good thermal stability in the current detectable range of 20–100 °C. These results imply that the cubic Gd_2O_3 upconversion nanoparticles may have multiplexing functionality in bio-imaging.

Introduction

Lanthanide-doped upconversion nanoparticles (UCNPs) are a promising optical functional species for the scientific community due to their unique spectroscopic properties and their potential applications in different fields.[1–12] Compared to semiconductor quantum dots and organic fluorophores, properties such as a high detection sensitivity, minimum photo-damage to biological materials, weak auto-fluorescence and a high penetration depth in living organisms or environmental samples allow UCNPs to be regarded as ideal luminescent candidates in the fields of bio-photonics and biomedical imaging.[13–19] In recent years, the development of inorganic functional nanoprobes with integrated magnetic and fluorescent characteristics has been receiving great attention. These materials hold great prospects for multiplexed bio-imaging, such as diagnostic analysis, real-time imaging and fluorescent labeling.[20] However, it is complex and difficult to bind two or more kinds of NPs with separate magnetic and optical functionalities into one nanosystem. To this end, it's a better choice to develop effective multifunctional NPs without adding any other moieties. From this point of view, Gd-based NPs (Gd_2O_2S, $NaGdF_4$, *etc.*) are promising multifunctional bio-probes that integrate optical and magnetic properties in a single phase.[21]

During the past decades, the Yb^{3+}–Er^{3+} sensitizer–activator pair has been recognized as an ideal lanthanide dopant for efficient upconversion luminescence. This pair usually shows two strong peaks of green emission which greatly limits the imaging penetration depth in tissues.[22,23] Red emission is relatively attractive for the optical imaging and simultaneous tracking of multiple biological species due to the wavelengths that are located in the first biological "optical window".[24,25] Scientists are devoted to achieving bright red upconversion luminescence using diverse approaches, *e.g.*, choosing host lattices, optimizing dopant concentrations, doping heterogeneous ions (Mn^{2+}, Fe^{3+}, *etc.*) and employing photonic crystals.[26–33] However, it remains a challenge to generate bright and pure red upconversion using a simple synthesis process and with multimodal functionality.

Herein, we report a succinct approach to control the red upconversion luminescence of Ln-doped (Ln = Er^{3+}, Yb^{3+}) Gd_2O_3 NPs which possess magnetic functionality due to the

[a]*College of Materials Science and Engineering, China Jiliang University, Hangzhou 310018, China. E-mail: zhzz85@zju.edu.cn; shiqingxu75@163.com*

[b]*College of Optical Science and Engineering, State Key Laboratory of Modern Optical Instrumentation, Zhejiang University, Hangzhou 310027, China*

† Electronic supplementary information (ESI) available: X-ray pattern and transmission electron microscopy of Gd_2O_2S. See DOI: 10.1039/c6ra22754f

Gd^{3+} ion. We synthesized the Gd_2O_3 NPs through calcining the Gd_2O_2S precursor with limited oxygen access. The structure, the formation process of the NPs, and the upconversion spectroscopic characteristics were investigated in detail. Comparative analysis of the Er^{3+} splitting transitions showed that the efficient cross relaxations between the Er^{3+} ions dominated the strong quasi-pure red upconversion luminescence in the Gd_2O_3–O_2 sample. It is expected that these NPs have potential applications in multimodal biomedical imaging because of their compatible optical and structural properties.

Experimental

Materials and methods

$GdCl_3 \cdot xH_2O$ (99.99%), $YbCl_3 \cdot 6H_2O$ (99.9%), $ErCl_3 \cdot 6H_2O$ (99.9%), 1-octadecene (ODE, 90%), oleic acid (OA, 90%), oleylamine (OM, 80–90%), sulfur (≥99.5%) and methanol (≥99.9%) were all purchased from Sigma-Aldrich. Acetylacetone was obtained from Aladdin. NaOH (AR), ethanol (AR) and cyclohexane (AR) were supplied by Sinopharm Chemical Reagent Company. All chemicals were used without further purification. Doubly distilled water was used in the experiment.

Synthesis of Gd_2O_2S:9% Yb^{3+},1% Er^{3+} nanoparticles

The synthesis of the Gd_2O_2S:9% Yb^{3+},1% Er^{3+} nanoparticles was similar to the previously reported protocol with some minor modifications.[34] $Ln(acac)_3 \cdot xH_2O$ (0.5 mmol), $Na(acac)_3 \cdot xH_2O$ (1.0 mmol), S (1.0 mmol), OA (2.5 mmol), OM (17 mmol) and ODE (20 mmol) were added in a three-neck flask (50 mL) at room temperature. The mixture was heated to 125 °C under vacuum for 3 h to obtain an optically clear solution. Then the temperature was raised to 315 °C at a rate of 20 °C min^{-1} under a highly purified Ar atmosphere and maintained at this temperature for 1 h. The solution was cooled down to room temperature, and the Gd_2O_2S:9% Yb^{3+},1% Er^{3+} nanoparticles were precipitated using absolute ethanol, followed by centrifugation and dried at 60 °C for 12 h.

Synthesis of Gd_2O_3:9% Yb^{3+},1% Er^{3+} nanoparticles

The Gd_2O_2S:9% Yb^{3+},1% Er^{3+} nanoparticles were used as the precursors for the preparation of the Gd_2O_3:9% Yb^{3+},1% Er^{3+} nanoparticles. The Gd_2O_2S:9% Yb^{3+},1% Er^{3+} precipitate was put into a small crucible, then calcined at 800 °C for 2 h under an N_2 (or ambient air) gas atmosphere with the heating rate of 4 °C min^{-1}, and then naturally cooled down to room temperature.

General characterization

The X-ray diffraction (XRD) pattern of Gd_2O_3:9% Yb^{3+},1% Er^{3+} was recorded using a Bruker D8 Advance X-ray diffraction system with Cu-Kα (1.5405 Å) radiation within a 25–65° range of 2θ. The shape and morphology of the samples were characterized using a SU8010 FE-SEM scanning electron microscope (HITACHI, Japan) and a FEI Tecnai G2 F20 S-WTINE transmission electron microscope. The TG-DTA curves were recorded using TGA/DSC 1LF1600 (METTLER-TOLEDO, Swit) with a rate of 4 °C min^{-1} under N_2 and ambient air. The Raman spectroscopy was performed using a 476G72 inVia-Reflex Raman Microscope (Renishaw, UK) under 785 nm excitation. The upconversion luminescence spectra were obtained with a PL3-211-P spectrometer (HORIBA JOBIN YVON, America) using a power-tunable 980 nm diode laser as the excitation source. For temperature dependent emissions, a TAP-02 temperature controller (ORIENT KOJI, China) was equipped to the spectrometer.

Results and discussion

Phase and morphology

Fig. 1(a) and (b) show the XRD patterns of the Gd_2O_3 NPs after calcinations in nitrogen (O_2-free) and ambient air (~21% O_2), and the corresponding samples are labelled as Gd_2O_3–O_2-free and Gd_2O_3–O_2, respectively. Gd_2O_2S NPs, which were prepared *via* a wet-chemical route, were used as precursors for the calcinations (see the ESI†). After annealing at 800 °C, the Gd_2O_3–O_2-free sample presented two crystal phases (Fig. 1(a)). The peaks can be directly indexed as cubic Gd_2O_3 (JCPDS no. 43-1014) and monoclinic Gd_2O_3 (JCPDS no. 42-1465). The XRD pattern of Gd_2O_3–O_2 is shown in Fig. 1(b), and the peaks can be indexed as a pure cubic phase of Gd_2O_3 (JCPDS no. 43-1014). TEM was utilized to characterize the morphology and structure of the NPs. From Fig. 1(c) and (d), the morphologies of the Gd_2O_3 NPs are slightly different due to the existence of the monoclinic phase in the Gd_2O_3–O_2-free sample. It can be seen that the obtained Gd_2O_3 displayed a nanosized polyhedron structure. The existence of monoclinic Gd_2O_3 NPs in the Gd_2O_3–O_2-free sample was confirmed by selective particle observation using high-resolution TEM, in which an interlayer spacing of 0.304 ± 0.01 nm was in good agreement with the *d* spacing of the (401) lattice plane of the monoclinic phase (Fig. 1(e)). The random observation of Gd_2O_3–O_2 revealed the unitary cubic phase, *e.g.*, the interlayer spacings of 0.312 nm, 0.411 nm, 0.185 nm and 0.254 nm are in accordance with the lattice spacing of the (222), (211), (433) and (411) planes of the cubic phase, respectively (Fig. 1(f)). These observations are in accordance with the XRD results.

Atmosphere controlled crystal formation

To investigate the formation dynamics of Gd_2O_3 from Gd_2O_2S, TG-DTA was performed. Fig. 2 shows the TG-DTA curves of Gd_2O_2S heated at a rate of 4 °C min^{-1} in different atmospheres. In the case of the O_2-free atmosphere (Fig. 2(a)), the formation of Gd_2O_3 can be roughly divided into three stages. The first stage with a weak weight loss is related to the evaporation of physically adsorbed and chemisorbed water in the temperature range of 30 °C to 300 °C.[17] The endothermic peaks at about 318 °C and 428 °C are accompanied by a second weight loss of 32% between 300 °C and 480 °C in the TG-DTA curves, which is in accordance with the decomposition of the crystal water and oxidation of the surface organic matter, respectively.[35] The weight loss (5%) above 480 °C indicates the decomposition from the intermediate phase to the oxide.[36] The strong exothermic peak is attributed to the decomposition of Gd_2O_2S at 580 °C.

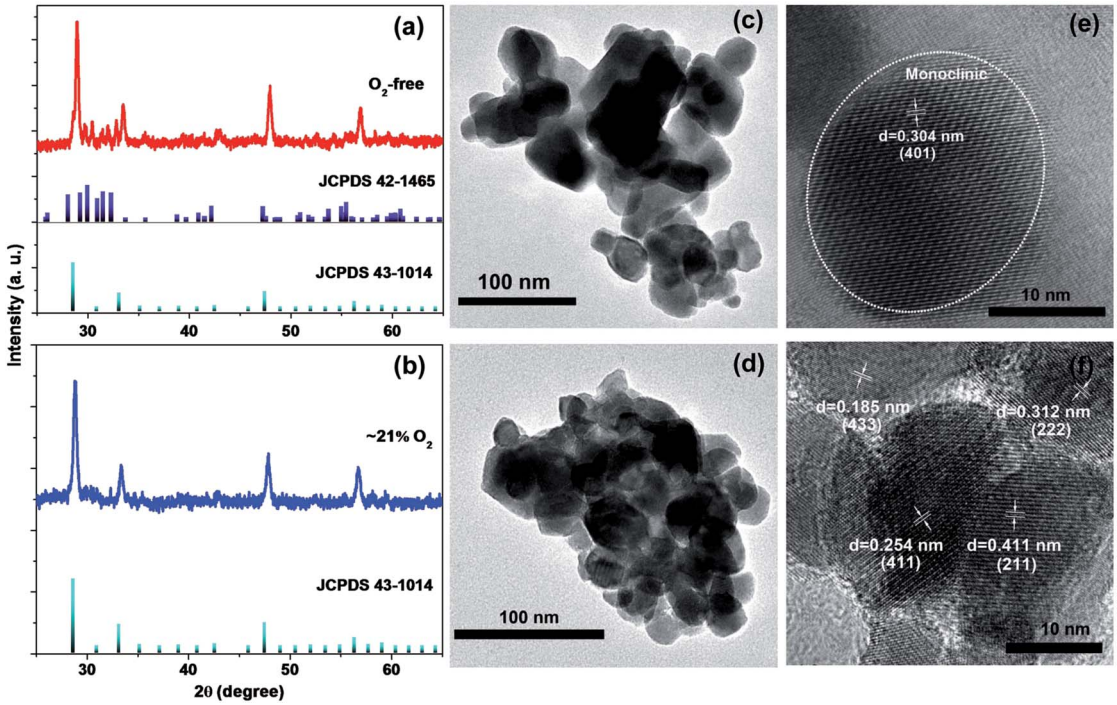

Fig. 1 Structures and morphologies of the nanoparticles. XRD patterns of (a) Gd_2O_3–O_2-free and (b) Gd_2O_3–O_2. TEM images of (c) Gd_2O_3–O_2-free and (d) Gd_2O_3–O_2. HRTEM images of (e) Gd_2O_3–O_2-free and (f) Gd_2O_3–O_2.

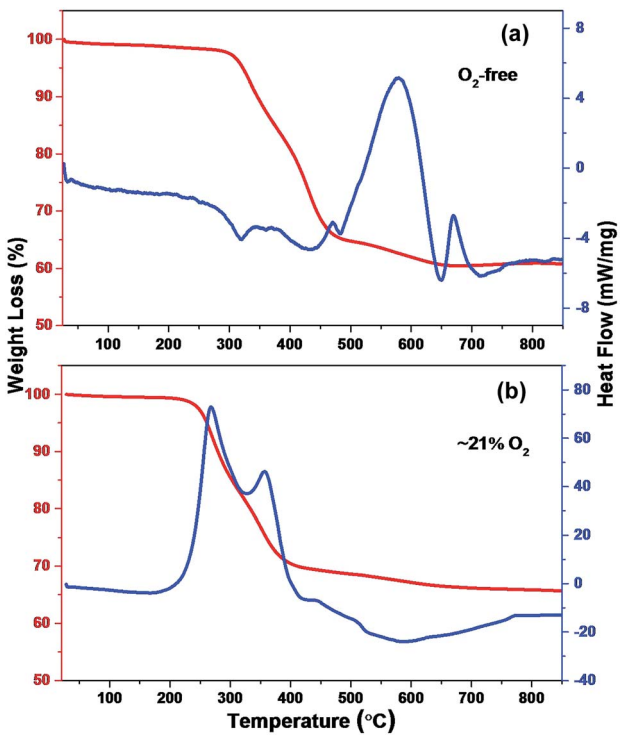

Fig. 2 TG-DTA curves of Gd_2O_2S synthesized under different atmospheres. (a) Sample calcined in N_2 at a heating rate of 4 °C min^{-1} and (b) sample calcined in ambient air at a heating rate of 4 °C min^{-1}.

The incomplete burning of decomposed organic materials produced the endothermic peak at 680 °C.[37] At the same time, the residual organic carbon reacted with the decomposed sulfur, which led to the conditions for the phase transition or induced the formation of the monoclinic phase Gd_2O_3. The reactions can be described by the following equations:

$$Gd_2O_2S \xrightarrow{580\ ^\circ C} Gd_2O_3 + S \quad (1)$$

$$C + 2S \rightarrow CS_2\uparrow \quad (2)$$

The reaction temperature noticeably decreases under aerobic conditions, which is shown in Fig. 2(b). It may be caused by a low content of oxygen vacancies in the formation of Gd_2O_3–O_2. A different vacancy content may lead to different phase transition and formation processes of the Gd_2O_3.[38] The first stage of weak weight loss stops at 240 °C in the formation of Gd_2O_3–O_2. There are two strong exothermic peaks at 270 °C and 360 °C, which are attributed to the oxidation of organic matter and the conversion from Gd_2O_2S to crystalline Gd_2O_3.[39] In the presence of oxygen, the sulphur oxides are oxidized to oxysulphate compounds at the temperature range of 500 °C to 600 °C. The weak endothermic peak at 585 °C and the mass loss (2%) between 410 °C and 750 °C are probably due to simultaneous occurrence of exothermic and endothermic reactions with a lack of net heat to produce a thermal event.[40] The reaction could be shown using the following equation:[41]

$$2Gd_2O_2S + 4O_2 \rightarrow 2Gd_2O_2SO_4 \rightarrow 2Gd_2O_3 + 2SO_2 + O_2 \quad (3)$$

After 750 °C, there are no heat fluctuations or weight losses in either sample, which indicates the accomplishment of

the decompositions and the formation of the Gd_2O_3 nanoparticles.

The Raman spectra of the two samples under 785 nm excitation are presented in Fig. 3. In the spectrum of the Gd_2O_3–O_2 sample, the bands located at 97, 118, 302 and 361 cm^{-1} are attributed to the cubic structure with a B_g stretching vibration, the bands at 145, 239, and 447 cm^{-1} are attributed to A_g stretching, and the bands at 402 and 561 cm^{-1} are attributed to the $A_g + B_g$ stretching.[42,43] In the spectrum of the Gd_2O_3–O_2-free sample, the peaks located at 70, 171, 250, 384, 483, 648 and 746 cm^{-1} are attributed to the host monoclinic Gd_2O_3. The other peaks located at 80, 97, 110, 413, 443 cm^{-1} arise from the cubic phase of Gd_2O_3.[44] The wavenumber values in Fig. 3 are a little different from the values reported in previous work. This may be caused by the phonon confinement effect in which nanoparticles can cause a frequency shift and the broadening of Raman peaks.

Upconversion luminescence

The comparative analyses of the upconversion luminescence behaviours for the two samples are shown in Fig. 4, in which a 980 nm laser diode with a power of 100 mW was employed as the excitation source. The faint green emissions peaking at the ordinary centre of 523 nm and 538 nm come from the $^2H_{11/2} \rightarrow {}^4I_{15/2}$ and $^4S_{3/2} \rightarrow {}^4I_{15/2}$ transitions of Er^{3+} ions, respectively. The dominating red emission originates from the Er^{3+}: $^4F_{9/2} \rightarrow {}^4I_{15/2}$ transition.[6,45] We can clearly observe three sets of splitting peaks for all the transitions, and we have chosen to label them in order of H_{1-4}, S_{1-3} and F_{1-7}, respectively. Apparently, the splitting transition probabilities of the two samples are totally different. This can be used as a fingerprint for identification of the lanthanides located in different crystal fields. The spectral profile of the Gd_2O_3–O_2 sample (blue lines in Fig. 4(a)) is confirmed in accordance with the Er^{3+} splitting peaks in the cubic lattice of Gd_2O_3.[46] The red lines of the Gd_2O_3–O_2-free sample indicate that most of the activated Er^{3+} ions have arisen from the monoclinic Gd_2O_3 lattice.[47]

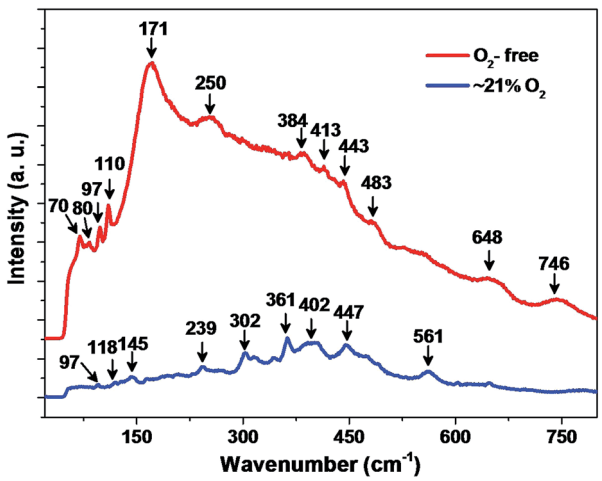

Fig. 3 Raman spectra of Gd_2O_3 nanoparticles which were calcined in different atmospheres.

Importantly, the green emission is nearly eliminated while the red emission is more efficient from the monoclinic phase to cubic phase.

To understand the upconversion mechanism, the excitation power (P) dependent upconversion (UC) emission intensity (I_{up}) of Gd_2O_3:Yb^{3+},Er^{3+} was measured. Fig. 4(c) and (d) demonstrate the dependence of I_{up} on P for Gd_2O_3:Yb^{3+},Er^{3+} under O_2-free and O_2 conditions, respectively. It is known that I_{up} is proportional to the power N of P, *i.e.*,[48]

$$I_{up} \propto P^N \Rightarrow \log(I_{up}) = \log(kP^N) = N \log P + A, \quad (4)$$

where N is the number of pump-photons required to populate the excited state and is determined by the slope of the fitted line. In Fig. 4(c)–(e), the slope values of 2.7, 2.7, 2.6 and 2.6 for the splitting states H_{1-4} and 2.5, 2.5 and 2.4 for the splitting states S_{1-3} are obtained, indicating that the population of the states $^2H_{11/2}$ and $^4S_{3/2}$ comes from the three-photon UC processes in the Gd_2O_3–O_2-free sample. The relatively smaller slopes that approach the value of 2 for H_{1-4} and S_{1-3} imply the corresponding two-photon UC processes in the Gd_2O_3–O_2 sample. The well-understood multiphoton population processes of Yb^{3+}–Er^{3+} energy transfer are described in Fig. 4(b). This population difference is due to the distinct phonon energy for the two phases, *e.g.*, the maximum phonon energy for the monoclinic phase (746 cm^{-1}) is much larger than the one for the cubic phase (561 cm^{-1}), as shown in Fig. 3. This induces a large probability of multiphonon relaxation for Er^{3+} in the monoclinic phase, *via* the following pathways: $^4I_{11/2} \cdots {}^4I_{13/2}$, $^4F_{9/2} \cdots {}^4I_{9/2} \cdots {}^4I_{11/2}$. For the red emission from the $^4F_{9/2}$ level, both of the samples have slopes corresponding to two-photon population upconversion. However, the cubic phase has a small slope for the $^4F_{9/2} \rightarrow {}^4I_{15/2}$ transition. This is due to the participation of cross relaxations including $(^4F_{7/2} + {}^4I_{11/2}) \rightarrow (^4F_{9/2} + {}^4F_{9/2})$ and $(^2H_{11/2} + {}^4I_{15/2}) \rightarrow (^4I_{9/2} + {}^4I_{13/2})$, which may have an excellent energy match in the cubic Gd_2O_3 sample.[49] The occurrence of the cross relaxations also helps us to understand why the cubic Gd_2O_3 phase has a more efficient population pathway (two-photon) for the $^2H_{11/2}$ and $^4S_{3/2}$ excited states of Er^{3+}, but has limited green emission.

Thermal stability

The thermal sensitivities of the Gd_2O_3:Yb^{3+},Er^{3+} nanoparticles over a temperature range of 20–100 °C were studied using the fluorescence intensity. From Fig. 5(a)–(c), the red emission decreased when increasing the temperature from 20 to 100 °C, which was in accordance with the classical theory of thermal quenching.[50] Quantitative temperature dependent intensity analysis in Fig. 5(c) shows that the Gd_2O_3–O_2 sample had better thermal stability than the Gd_2O_3–O_2-free sample. The stability of the lanthanide-doped sesquioxides can be understood in terms of the phonon energy difference between the two phases. According to the multiphonon relaxation rate:[51]

$$W_{mp}(T) = W_{mp}(0)(1 - e^{-\hbar w_{max}/kT})^{-p} \quad (5)$$

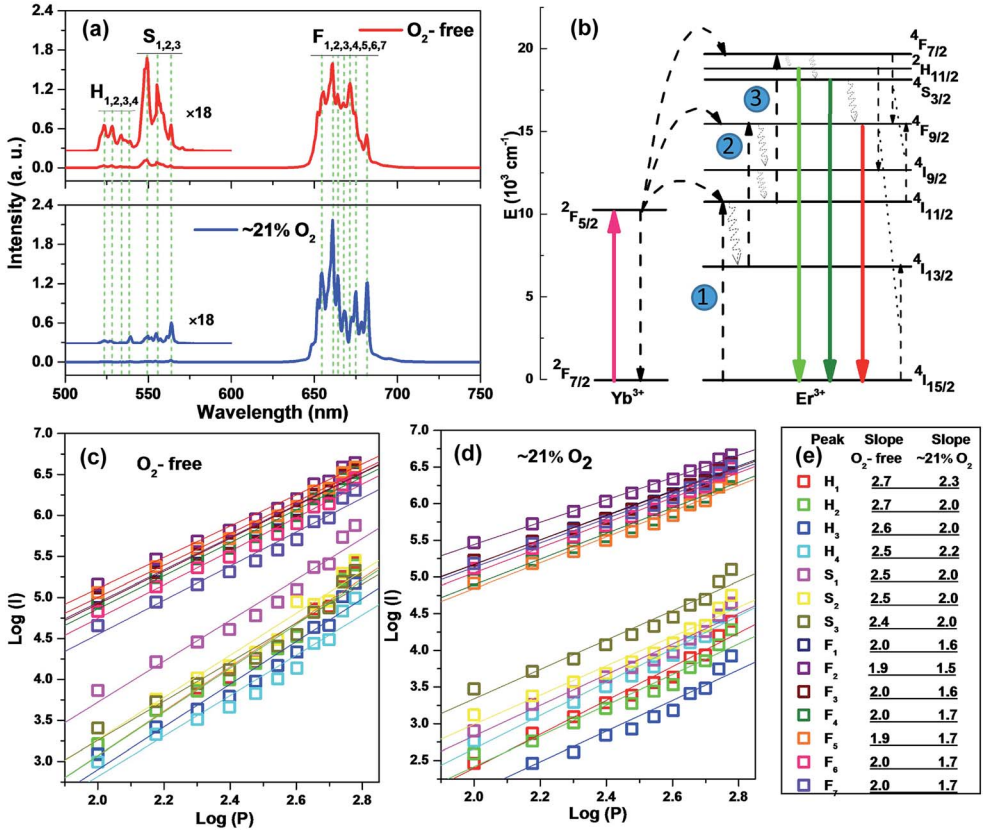

Fig. 4 (a) Room temperature upconversion luminescence spectra of Gd_2O_3:Yb^{3+},Er^{3+} under different calcination conditions. (b) Proposed energy transfer mechanisms showing the upconversion processes in Gd_2O_3:Yb^{3+},Er^{3+} nanoparticles under 980 nm laser excitation. Double-logarithmic plots of the excitation power dependent emission intensity of (c) the sample calcined in N_2, and (d) the sample calcined in ambient air. (e) The specific slope values of the different splitting transitions in the two samples.

where p is the number of phonons and W_{mp} is the relaxation rate of 0 K, lower phonon energy leads to a lower multiphonon relaxation rate, and consequently to a higher thermal stability. It is suggested that the Gd_2O_3–O_2 sample is less sensitive to temperature, which is more beneficial for applications because it is little affected by the changing of external fields.

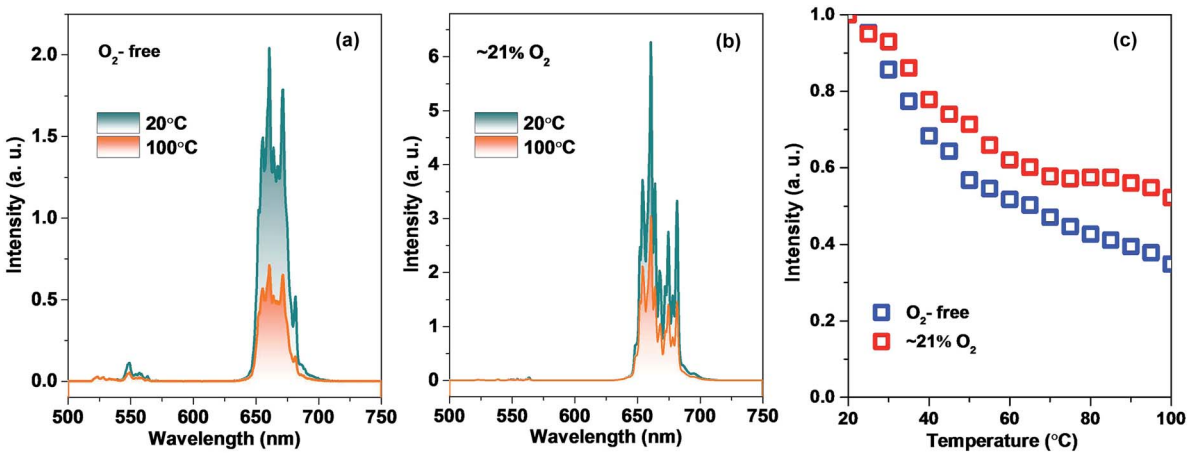

Fig. 5 Temperature-dependent luminescence of Gd_2O_3:Yb^{3+},Er^{3+} nanoparticles between 20 °C and 100 °C (excitation at 980 nm). Emission spectra for the sample (a) calcined in N_2, and (b) calcined in ambient air. (c) Relative intensity changing tendencies of the two samples with increasing temperature.

Conclusions

In conclusion, we successfully controlled the phase of Gd_2O_3 by calcining a Gd_2O_2S precursor in an O_2 limited atmosphere. The TG-DTA curves demonstrated the different formation of the Gd_2O_2S:Yb^{3+},Er^{3+} under different atmospheres, in which a high oxygen content can induce a pure cubic phase. Obvious splitting of the electronic transitions was observed in the Gd_2O_3 NPs, which emitted much stronger red light than green light. The cubic Gd_2O_3 phase is beneficial for the pure red upconversion, because of the lower maximum phonon energy, moderate multiphonon relaxations and cross relaxations. Also, the cubic Gd_2O_3 UC nanoparticles displayed a high thermal stability in terms of the luminescence intensity over a temperature range of 20–100 °C, which is more beneficial for application in multi-modality biomedical imaging and NIR light-triggered photodynamic therapy.

Acknowledgements

The authors acknowledge financial support from Zhejiang Provincial Natural Science Foundation of China (No. LY14E020007, LQ14E020005, LY17E020007) and National Natural Science Foundation of China (No. 11404311, 11304202).

Notes and references

1 B. Zhou, B. Y. Shi, D. Y. Jin and X. G. Liu, *Nat. Nanotechnol.*, 2015, **10**, 924–936.
2 J. B. Zhao, D. Y. Jin, E. P. Schartner, Y. Q. Lu, Y. J. Liu, A. V. Zvyagin, L. X. Zhang, J. M. Dawes, P. Xi, J. A. Piper, E. M. Goldys and T. M. Monro, *Nat. Nanotechnol.*, 2013, **8**, 729–734.
3 X. S. Yang, H. Xie, E. Alonas, Y. J. Liu, X. Z. Chen, P. J. Santangelo, Q. S. Ren, P. Xi and D. Y. Jin, *Light: Sci. Appl.*, 2016, **5**, e16134.
4 D. M. Liu, X. X. Xu, Y. Du, X. Qin, Y. H. Zhang, C. S. Ma, S. H. Wen, W. Ren, E. M. Goldys, J. A. Piper, S. X. Dou, X. G. Liu and D. Y. Jin, *Nat. Commun.*, 2016, **7**, 10254–10262.
5 M. K. Gnanasammandhan, N. M. Idris, A. Bansal, K. Huang and Y. Zhang, *Nat. Protoc.*, 2016, **11**, 688–713.
6 F. Wang, Y. Han, C. S. Lim, Y. H. Lu, J. Wang, J. Xu, H. Y. Chen, C. Zhang, M. H. Hong and X. G. Liu, *Nature*, 2010, **463**, 1061–1065.
7 J. Wang, R. R. Deng, M. A. MacDonald, B. L. Chen, J. K. Yuan, F. Wang, D. Z. Chi, T. S. A. Hor, P. Zhang, G. K. Liu, Y. Han and X. G. Liu, *Nat. Mater.*, 2014, **13**, 157–162.
8 D. Pile, *Nat. Photonics*, 2013, **7**, 348–349.
9 H. Xu, R. F. Chen, Q. Sun, W. Y. Lai, Q. Q. Su, W. Huang and X. G. Liu, *Chem. Soc. Rev.*, 2014, **43**, 3259–3302.
10 F. Wang and X. G. Liu, *Chem. Soc. Rev.*, 2009, **38**, 976–989.
11 N. M. Idris, M. K. Jayakumar, A. Bansal and Y. Zhang, *Chem. Soc. Rev.*, 2015, **44**, 1449–1478.
12 X. Y. Huang, S. Y. Han, W. Huang and X. G. Liu, *Chem. Soc. Rev.*, 2013, **42**, 173–201.
13 J. Zhou, Z. Liu and F. Y. Li, *Chem. Soc. Rev.*, 2012, **41**, 1323–1349.
14 Y. H. Zhang, L. X. Zhang, R. R. Deng, J. Tian, Y. Zong, D. Y. Jin and X. G. Liu, *J. Am. Chem. Soc.*, 2014, **136**, 4893–4896.
15 F. Wang and X. G. Liu, *J. Am. Chem. Soc.*, 2008, **130**, 5642–5643.
16 C. L. Yan, A. Dadvand, F. Rosei and D. F. Perepichka, *J. Am. Chem. Soc.*, 2010, **132**, 8868–8869.
17 B. Antic, J. Rogan, A. Kremenovic, A. S. Nikolic, M. Vucinic-Vasic, D. K. Bozanic, G. F. Goya and P. H. Colomban, *Nanotechnology*, 2010, **21**, 245702–245709.
18 L. Zhou, R. Wang, C. Yao, X. M. Li, C. L. Wang, X. Y. Zhang, C. L. Xu, A. J. Zeng, D. Y. Zhao and F. Zhang, *Nat. Commun.*, 2015, **6**, 6938–6948.
19 H. M. Zhu, C. C. Lin, W. Q. Luo, S. T. Shu, Z. G. Liu, Y. S. Liu, J. T. Kong, E. Ma, Y. G. Cao, R. S. Liu and X. Y. Chen, *Nat. Commun.*, 2014, **5**, 4312–4322.
20 S. S. Yang, H. Gao, Y. F. Wang, S. Y. Xin, Y. M. He, Y. Z. Wang and W. Zeng, *Mater. Res. Bull.*, 2013, **48**, 37–40.
21 L. J. Zhou, Z. J. Gu, X. X. Liu, W. Y. Yin, G. Tian, L. Yan, S. Jin, W. L. Ren, G. M. Xing, W. Li, X. L. Chang, Z. B. Hu and Y. L. Zhao, *J. Mater. Chem.*, 2012, **22**, 966–974.
22 Y. H. Hu, X. H. Liang, Y. B. Wang, E. Z. Liu, X. Y. Hu and J. Fan, *Ceram. Int.*, 2015, **41**, 14545–14553.
23 J. H. Zeng, J. Su, Z. H. Li, R. X. Yan and Y. D. Li, *Adv. Mater.*, 2005, **17**, 2119–2123.
24 D. Q. Chen, Y. Chen, H. W. Lu and Z. G. Ji, *Inorg. Chem.*, 2014, **53**, 8638–8645.
25 Z. Yang, P. C. Lin, C. F. Guo and W. R. Liu, *RSC Adv.*, 2015, **5**, 13184–13191.
26 G. P. Dong, B. B. Chen, X. D. Xiao, G. Q. Chai, Q. M. Liang, M. Y. Peng and J. R. Qiu, *Nanoscale*, 2012, **4**, 4658–4666.
27 J. Y. Liao, Z. W. Yang, H. J. Wu, D. Yan, J. B. Qiu, Z. G. Song, Y. Yang, D. C. Zhou and Z. Y. Yin, *J. Mater. Chem. C*, 2013, **1**, 6541–6546.
28 H. Shibata, K. Imakita and M. Fujii, *RSC Adv.*, 2014, **4**, 32293–32297.
29 B. Shao, Z. W. Yang, Y. D. Wang, J. Li, J. Z. Yang, J. B. Qiu and Z. G. Song, *ACS Appl. Mater. Interfaces*, 2015, **7**, 25211–25218.
30 J. Tang, L. Chen, J. Li, Z. Wang, J. H. Zhang, L. G. Zhang, Y. S. Luo and X. J. Wang, *Nanoscale*, 2015, **7**, 14752–14759.
31 S. Y. Ye, Y. H. Zhang, H. L. He, J. R. Qiu and G. P. Dong, *J. Mater. Chem. C*, 2015, **3**, 2886–2896.
32 T. Wen, Y. N. Zhou, Y. Z. Guo, C. M. Zhao, B. C. Yang and Y. G. Wang, *J. Mater. Chem. C*, 2016, **4**, 684–690.
33 Y. Zhou, Z. J. Yong, K. C. Zhang, B. M. Liu, Z. W. Wang, J. S. Hou, Y. Z. Fang, Y. Zhou, H. T. Sun and B. Song, *J. Phys. Chem. Lett.*, 2016, **7**, 2735–2741.
34 T. Zhang, J. Gu, Y. Ding, Y. W. Zhang and C. H. Yan, *ChemPlusChem*, 2013, **78**, 515–521.
35 J. Chandradass, M. Balasubramanian, D. S. Bae and H. Kim, *Mater. Manuf. Processes*, 2012, **27**, 1290–1294.
36 Y. Gao, Q. Zhao, Q. H. Fang and Z. H. Xu, *Dalton Trans.*, 2013, **42**, 11082–11091.
37 G. X. Ping, X. Y. Wang, Y. T. Wu, L. S. Qin and K. Y. Shu, *Opt. Mater.*, 2012, **34**, 748–752.

38 A. Kossoy, Y. Feldman, R. Korobko, E. Wachtel, I. Lubomirsky and J. Maier, *Adv. Funct. Mater.*, 2009, **19**, 634–641.
39 M. L. Dos Santos, R. C. Lima, C. S. Riccardi, R. L. Tranquilin, P. R. Bueno, J. A. Varela and E. Longo, *Mater. Lett.*, 2008, **62**, 4509–4511.
40 J. B. Lian, X. D. Sun, T. Gao, Q. Li, X. D. Li and Z. G. Liu, *J. Mater. Sci. Technol.*, 2009, **25**, 254–258.
41 J. Bang, M. Abboudi, B. Abrams and P. H. Holloway, *J. Lumin.*, 2004, **106**, 177–185.
42 C. Le Luyer, A. García-Murillo, E. Bernstein and J. Mugnier, *J. Raman Spectrosc.*, 2003, **34**, 234–239.
43 J. Q. Yu, L. Cui, H. Q. He, S. H. Yan, Y. S. Hu and H. Wu, *J. Rare Earths*, 2014, **32**, 1–4.
44 N. Paul, M. Devi and D. Mohanta, *Mater. Res. Bul.*, 2011, **46**, 1296–1300.
45 J. W. Zhao, Y. J. Sun, X. G. Kong, L. J. Tian, Y. Wang, L. P. Tu, J. L. Zhao and H. Zhang, *J. Phys. Chem. B*, 2008, **112**, 15666–15672.
46 H. Guo, N. Dong, M. Yin, W. P. Zhang, L. R. Lou and S. D. Xia, *J. Phys. Chem. B*, 2004, **108**, 19205–19209.
47 J. Liu, H. W. Deng, Z. Huang, Y. L. Zhang, D. H. Chen and Y. Z. Shao, *Phys. Chem. Chem. Phys.*, 2015, **17**, 15412–15418.
48 H. Li, S. X. Song, W. Wang and K. Z. Chen, *Dalton Trans.*, 2015, **44**, 16081–16090.
49 W. Wei, Y. Zhang, R. Chen, J. L. Goggi, N. Ren, L. Huang, K. K. Bhakoo, H. D. Sun and T. T. Y. Tan, *Chem. Mater.*, 2014, **26**, 5183–5186.
50 B. S. Cao, J. L. Wu, X. H. Wang, Y. Y. He, Z. Q. Feng and B. Dong, *Sensors*, 2015, **15**, 30981–30990.
51 T. T. Basiev, Y. V. Orlovskii, K. K. Pukhov, V. B. Sigachev, M. E. Doroshenko and I. N. Vorob'ev, *J. Lumin.*, 1996, **68**, 241–253.